Open access • Journal Article • DOI:10.1088/0004-637X/801/2/83

Homologous Helical Jets: Observations by IRIS, SDO and Hinode and Magnetic Modeling with Data-Driven Simulations — Source link

Mark C. M. Cheung, B. De Pontieu, T. D. Tarbell, Yixing Fu ...+17 more authors

Published on: 07 Jan 2015 - arXiv: Solar and Stellar Astrophysics

THE ASTROPHYSICAL JOURNAL, 801:83 (13pp), 2015 March 10 doi:10.1088/0004-637X/801/2/83

HOMOLOGOUS HELICAL JETS: OBSERVATIONS BY *IRIS*, *SDO*, AND *HINODE* AND MAGNETIC MODELING WITH DATA-DRIVEN SIMULATIONS

MARK C. M. CHEUNG[1], B. DE PONTIEU[1,2], T. D. TARBELL[1], Y. FU[1,3], H. TIAN[4], P. TESTA[4], K. K. REEVES[4], J. MARTÍNEZ-SYKORA[1,5], P. BOERNER[1], J. P. WÜLSER[1], J. LEMEN[1], A. M. TITLE[1], N. HURLBURT[1], L. KLEINT[6], C. KANKELBORG[7], S. JAEGGLI[7], L. GOLUB[4], S. MCKILLOP[4], S. SAAR[4], M. CARLSSON[2], AND V. HANSTEEN[2]
[1] Lockheed Martin Solar and Astrophysics Laboratory, 3251 Hanover Street Bldg. 252, Palo Alto, CA 94304, USA; cheung@lmsal.com
[2] Institute of Theoretical Astrophysics, University of Oslo, P.O. Box 1029, Blindern, NO-0315 Oslo, Norway
[3] Space Sciences Laboratory, University of California, Berkeley, 7 Gauss Way, Berkeley, CA 94720, USA
[4] Harvard-Smithsonian Center for Astrophysics, 60 Garden Street, Cambridge, MA 02138, USA
[5] Bay Area Environmental Research Institute, 625 2nd St. Ste 209, Petaluma, CA 94952, USA
[6] University of Applied Sciences and Arts Northwestern Switzerland, Bahnhofstr. 6, 5210 Windisch, Switzerland
[7] Department of Physics, Montana State University, Bozeman, P.O. Box 173840, Bozeman, MT 59717, USA
Received 2014 October 15; accepted 2015 January 7; published 2015 March 5

ABSTRACT

We report on observations of recurrent jets by instruments on board the *Interface Region Imaging Spectrograph*, *Solar Dynamics Observatory* (*SDO*), and *Hinode* spacecraft. Over a 4 hr period on 2013 July 21, recurrent coronal jets were observed to emanate from NOAA Active Region 11793. Far-ultraviolet spectra probing plasma at transition region temperatures show evidence of oppositely directed flows with components reaching Doppler velocities of ±100 km s^{-1}. Raster Doppler maps using a Si IV transition region line show all four jets to have helical motion of the same sense. Simultaneous observations of the region by *SDO* and *Hinode* show that the jets emanate from a source region comprising a pore embedded in the interior of a supergranule. The parasitic pore has opposite polarity flux compared to the surrounding network field. This leads to a spine-fan magnetic topology in the coronal field that is amenable to jet formation. Time-dependent data-driven simulations are used to investigate the underlying drivers for the jets. These numerical experiments show that the emergence of current-carrying magnetic field in the vicinity of the pore supplies the magnetic twist needed for recurrent helical jet formation.

Key words: magnetic fields – Sun: atmosphere – Sun: chromosphere – Sun: corona – Sun: photosphere – Sun: transition region

Supporting material: animation

1. INTRODUCTION

Since the discovery of coronal jets in X-ray (e.g., Shibata et al. 1992) and EUV (e.g., Chae et al. 1999) imaging observations, there has been a growing body of observational and theoretical work investigating the physical mechanisms behind this phenomenon. While the detailed physical processes responsible for the acceleration of jet material depends on the local conditions (e.g., see Takasao et al. 2013), there is overwhelming evidence that magnetic reconnection is key for the impulsive energy release associated with jets. As for the driving mechanism that allows for energy build up, it has been reported that many jets are associated with emerging flux and/or flux cancellation events in the photosphere. In the case of recurrent jets (e.g., Chae et al. 1999; Chifor et al. 2008; Guo et al. 2013; Schmieder et al. 2013; Chandra et al. 2015) emanating from the same source region on the Sun, an additional question is how the underlying driver leads to magnetic configurations that repeatedly erupt to produce jets of a homologous nature.

We address the question posed above by performing a study of recurrent jets observed by multiple spaceborne observatories and by using data-driven simulations. The rest of the article is structured as follows. Section 2 presents observations of the jets in the transition region and corona by the Atmospheric Imaging Assembly (AIA; Boerner et al. 2012; Lemen et al. 2012) on board the *Solar Dynamics Observatory* (*SDO*; Pesnell et al. 2012) and by the *Interface Region Imaging Spectrograph* (*IRIS*; De Pontieu et al. 2014). Section 3 presents photospheric observations in and around the source region of the jets by the Solar Optical Telescope (SOT; Tsuneta et al. 2008) on board the *Hinode* spacecraft (Kosugi et al. 2007).

Section 4.1 describes the evolution of the photospheric field in the region of interest as revealed by vector magnetograms from the Helioseismic and Magnetic Imager (HMI; Scherrer et al. 2012; Schou et al. 2012) on board *SDO*. Section 4.2 presents results from simulations of coronal and chromospheric field evolution driven by HMI vector magnetograms. The physical implications of this study are discussed in Section 5.

2. OBSERVATIONAL EVIDENCE FOR HOMOLOGOUS, HELICAL JETS

The recurrent jets and the source region of these jets were simultaneously observed by *IRIS*, *SDO*, and *Hinode*. Instruments on board these satellites provide complementary coverage in wavelength, temperature, and spatiotemporal domains. Together they present an integrated picture of the magnetic and atmospheric environment responsible for driving and initiating the set of recurrent jets. The following sections discuss observations of the region of interest as seen by the various instruments.

2.1. Photospheric and Coronal Observations by SDO

Continuous full disk observations from *SDO* provide context about the environment in which the recurrent jets are generated.

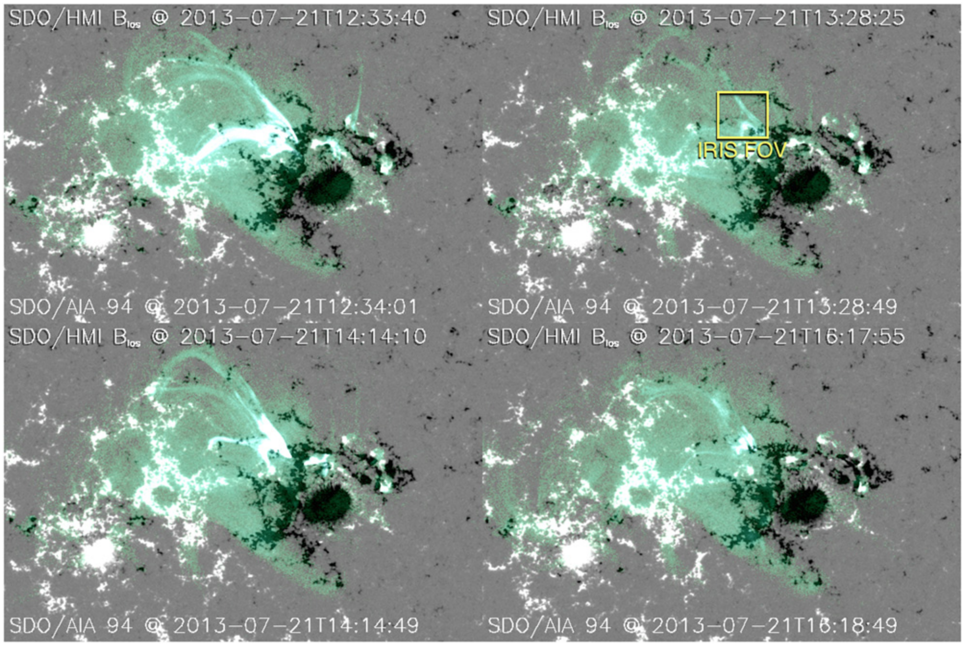

Figure 1. HMI line of sight magnetograms (grayscale) overlaid with AIA 94 Å channel images of the four recurrent jets. The ejecta from the jets are channeled into closed loops connected the leading and trailing polarities of AR 11793. The yellow box in the top right panel shows the field of view of *IRIS* slit-jaw images.

(An animation of this figure is available.)

Figure 1 shows the large-scale structure of active region (AR) 11793 in the time period during which *IRIS* observed the recurrent jets. During this time range the AR is roughly centered at a Stonyhurst longitude and latitude of W11 and N23 deg, respectively.

We refer to each of the four observed jets as J1, J2, J3, and J4 in chronological order. The four jets are shown in separate panels of Figure 1. Each panel consists of an HMI line of sight (LOS) magnetogram (from the `hmi.M_45s` data series) overlaid with an EUV image from the AIA 94 Å channel. The `aia_prep.pro` routine in SolarSoft was used to align the full disk images from the two instruments and to remap them to a common plate-scale of 0.6 arcsec per pixel. Inspection of the overlaid images (and accompanying animation) reveals that the jets emanate from a strong plage region in the northeastern edge of the leading (negative) polarity patch of the AR.

Though the jets are not identical, they possess strikingly similar features. First of all, the ejecta in the jets are channeled into closed loops connecting the leading and trailing polarities of the AR. This is unlike some jets found in coronal hole regions, in which jet material is channeled into open magnetic field lines (e.g., Cirtain et al. 2007; Savcheva et al. 2007; Moreno-Insertis et al. 2008; Patsourakos et al. 2008). Second, each of the jet events can be considered to possess a two-part structure, namely, the inclined jet itself accompanied by the brightening of a compact closed loop (or multiple closed loops) adjacent to the jet (Shibata et al. 1994; Shimojo et al. 1996). It is worth noting that the jets can also be identified in the other EUV channels. This likely implies that they have a multi-thermal structure.

In all four cases, the footpoints of the bright compact loops closest to the jets are found in the negative polarity network whereas the conjugate footpoints are located at a parasitic polarity patch within an adjacent supergranule. We will discuss the magnetic configuration of the environment around the jets in Sections 3 and 4.

2.2. Transition Region Observations by *IRIS*

Between 11:34 and 16:34 UTC on 2013 July 21, *IRIS* ran a medium coarse 20 step raster observation program with 150 repeats on the region of interest. The field of view (FOV) of the slit-jaw images (SJIs) is $60'' \times 60''$and the approximate pointing is indicated by the yellow box in the top right panel of Figure 1. The raster step size is $2''$ so each spectral raster spans an FOV of $38'' \times 60''$. Each repeat of a spectral raster is accompanied by five SJIs in each of the C II 1330, Si IV 1400, and Mg II k 2796 channels and one continuum image in 2832. Level 2 data were used for all of the following analyses. SJIs in the level 2 data product are dark-subtracted, flatfielded, and geometrically corrected so that images from different channels are on a common grid. The same corrections are applied to near-ultraviolet and far-ultraviolet (FUV) spectra. Furthermore, the spectra are stacked as 3D raster cubes for convenient analysis.

Figure 2 shows a Si IV 1400 SJI of J1. The spectrograph samples along the vertical dark slit at $x = 154$ arcsec FUV spectral line profiles are plotted for three different positions indicated by the blue, green, and red cursors straddling the jet in the SJI. We first inspect the profiles of the Si IV lines at 1393.8 and 1402.8 Å. Both are transition region lines that form at $\log T/K \sim 4.9$ (from CHIANTI 7.0; Landi et al. 2012). For this reason, the shapes of the line profiles are very similar. By visual inspection, it can be discerned that the Si IV line profiles at the three positions have very different bulk Doppler shifts. While the centroids of the blue and green profiles have blueshifts of $\approx$80 and 30 km s^{-1}, respectively, the centroid of the red profile is clearly redshifted. The spectral profiles at all three locations have wide wings with contributions beyond ± 100 km s^{-1} relative to the centroid positions. The spectral readout window of the Si IV 1403 spectra includes

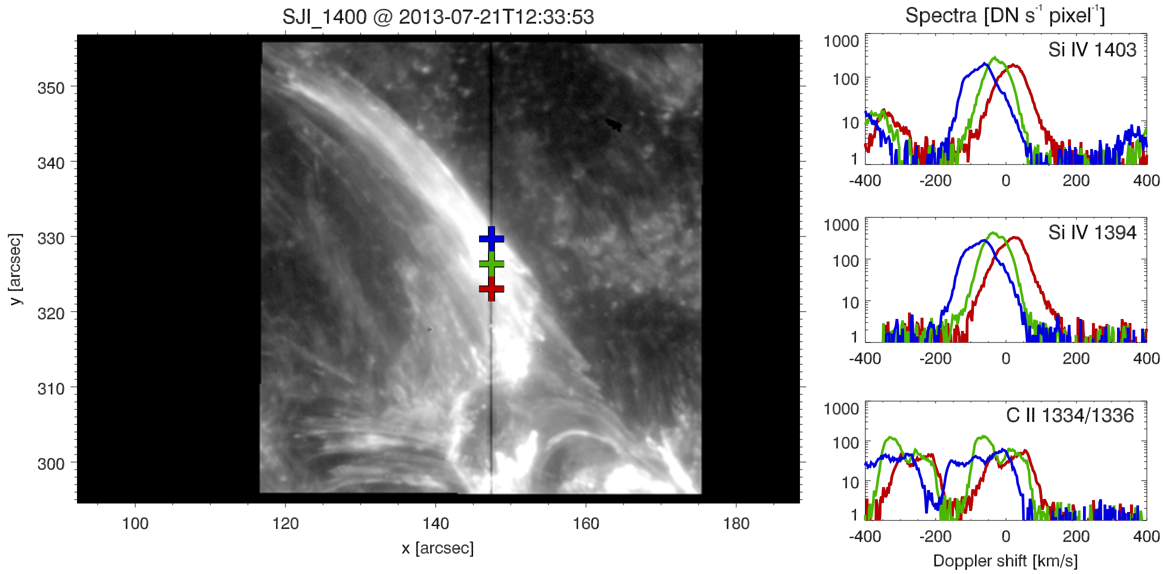

Figure 2. Left: Si IV 1400 slit-jaw image of the first recurrent jet. Right: Spectral line profiles sampled at the blue, green, and red cursor positions (all lying on the vertical slit) for Si IV 1403, Si IV 1394, and the pair of C II lines at 1334 and 1336 (the rest wavelength of the latter is used as a reference). The spectra are plotted as functions of Doppler shift from their respective rest wavelengths.

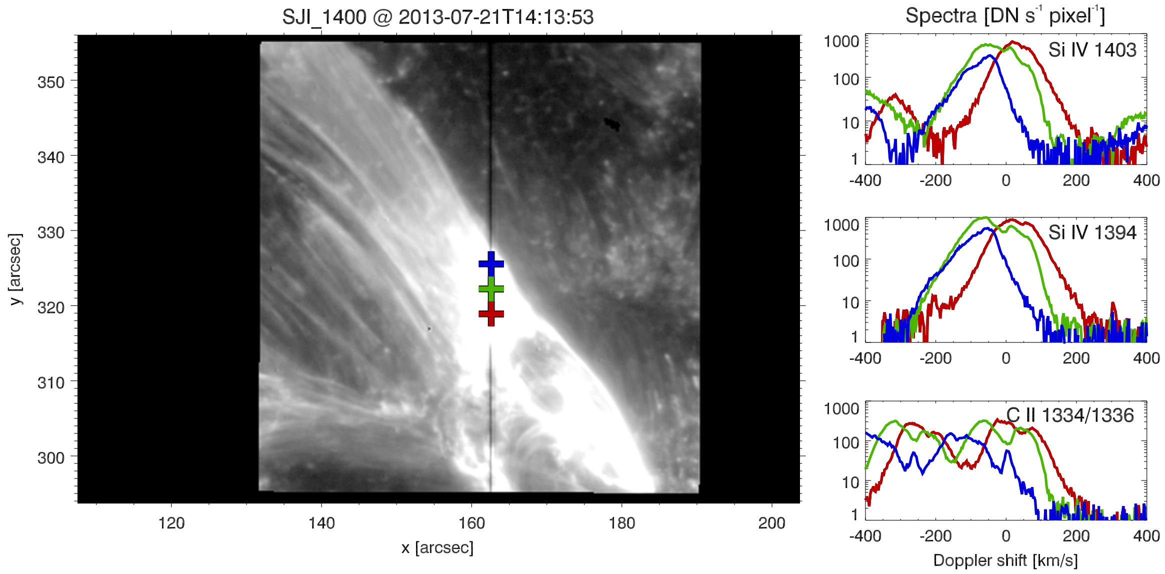

Figure 3. Same as Figure 2 but for the third jet. The FUV profiles in this case are even broader, with lines having contributions from up to ±200 km s^{-1} Doppler shifts relative to the centroids.

the O IV 1401 line, which forms at log $T \sim 5.2$. The signal from this line appears in the plotted Si IV 1403 spectra at Doppler shifts beyond -300 km s^{-1}.

The bottom panel of the right column in Figure 2 shows spectra for the C II lines, which are expected to form at log $T/K \sim 4.4$ (from CHIANTI 7.0; Landi et al. 2012). In the plots the rest wavelength of the red line (1335.71 Å) was used to calculate the effective Doppler shift. The shapes of the C II lines are much more complex than those of the Si IV lines. The profiles at the green and red cursor positions are bimodal. However, the green profile has a higher amplitude peak on the blue side of the line while the red line has a higher amplitude peak on the red side. Even more complex is the blue profile, which has a trimodal shape. One may initially be tempted to interpret the bimodal profiles in terms of oppositely directed Doppler flows. However, we caution that the C II lines are usually optically thick, so the dip in bimodal (or trimodal) line profiles likely results from opacity effects.

Figure 3 is similar to Figure 2 but for J3. There are many qualitative similarities between the profiles in these jets. For instance the red and blue colored profiles here show bulk red- and blueshifts, respectively. In the case of J3, the lines are even broader (with contributions up to ±200 km s^{-1} relative to the centroid position) and the pair of C II lines are now completely blended. The green profiles for the Si IV lines in Figure 3 show a bimodal structure. This is probably different from the two-component spectral profiles studied by Tian et al. (2012) in their study of EUV jets. In their case, they performed a double Gaussian fit to spectral profiles taken by the EUV Imaging Spectrograph instrument on board *Hinode* and found that one component corresponds to steady background emission, while a blueshifted second component is attributed to outflows from

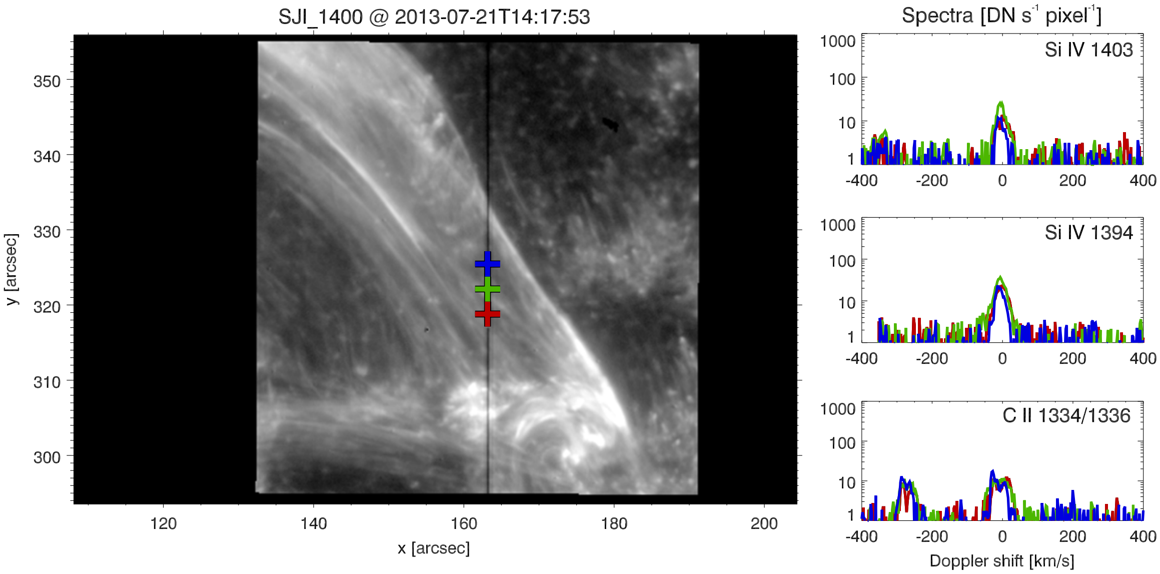

Figure 4. Same as Figure 3 but four minutes later. The jet has already subsided and the FUV profiles are also much narrower than during the impulsive phase of the jet.

the jet. In our case (green Si IV 1394 profile in Figure 3), one component has a bulk redshift while the other component has a bulk blueshift. Inspection of corresponding profiles at positions north and south of this location (i.e., as indicated by the blue and red cursors on the SJI) shows the profile to the north has a blueshifted component, while the profile to the south has a redshifted component. Since the profile sampled at the position of the green cursor is midway between the two, it is not surprising that the green spectral profile has both red- and blueshifted components. In contrast, the FUV line profiles in the post-impulsive phase (four minutes later; see Figure 4) are dimmer by almost two orders of magnitude, are much narrower, and have zero mean Doppler shift.

The FUV line profiles for different locations spanning the widths of J1 and J3 both indicate a bulk blueshift near the northern edge of the jet and a bulk redshift near its southern edge. Using raster scans, we investigate whether this is a pattern that pertains to all four jets. As per the above discussion, the Si IV 1394 line is simplest to analyze. Using this line, we calculate the zeroth and first moments

$$I_{\rm line} = \int dI \qquad (1)$$

$$\langle v_{\rm line} \rangle = I_{\rm line}^{-1} \int I dv_{\rm los}, \qquad (2)$$

where I is the spectrograph intensity (in DN sec^{-1} pixel^{-1}) and $v_{\rm los}$ is the LOS Doppler velocity. $I_{\rm line}$ is simply the integrated intensity across the line. Over the FOV of the *IRIS* rasters, the ratio I_{1394}/I_{1403} is generally close to the theoretical value of 1.95 as predicted using CHIANTI (Landi et al. 2012), which suggests the Si IV lines are optically thin. Adopting this assumption, we interpret $\langle v_{\rm line} \rangle$ to be an intensity-weighted mean Doppler velocity.

Figure 5 shows raster maps of $I_{\rm line}$ and $\langle v_{\rm line} \rangle$ for the Si IV 1394 line for all four jets. While the amplitude of $\langle v_{\rm line} \rangle$ is larger in some jets than others, all four jets tend to have blue- and redshifts at their upper (northern) and lower edges (southern), respectively. This type of spatial pattern in Doppler maps have previously been detected in individual jets (Pike & Mason 1998) and surges (Curdt & Tian 2011). While Pike & Mason (1998) used data from the Coronal Diagnostic Spectrometer (CDS, Harrison et al. 1995) and Curdt & Tian (2011) used data from the Solar Ultraviolet Measurements of Emitted Radiation (Wilhelm et al. 1995) instrument, both studies used the same O V transition region line, which forms at $\log T/K \sim 5.4$. In both studies, the spatial pattern of Doppler shifts was taken as evidence for helical motion. We adopt the same interpretation and take our *IRIS* Doppler maps as evidence for helical motion in all four of the recurrent jets. In a local Cartesian reference frame where $\hat{l}$ points along the jet (increasing height), the spatial pattern of $\langle v_{\rm line} \rangle$ corresponds to rotational motion with vorticity $\omega_l = (\nabla \times \boldsymbol{v})_l < 0$. This implies the kinetic helicity of plasma motion associated with the jet is $u_l\, \omega_l < 0$ (by definition, u_l is positive since it is the component of plasma flow along the jet direction).

O IV lines observed in *IRIS* FUV spectra allow us to perform density diagnostics on the jet material. We used two different line ratios to measure the densities. The first is the ratio of the O IV 1401.1 and 1404.8 lines. The 1404.8 line is blended with a S IV line, so we used the S IV 1406.02 line and the assumption of optically thin emission to extract the intensity of O IV 1404.8. The O IV 1404.8 line is not always present in the spectral readout window of *IRIS*. However, in a number of slit positions where there is sufficient blueshift, we find the ratio O IV 1401.1/1404.8 to be in the range 4.0–4.5. For a temperature range of $\log T/K = 4.5$–5.5 (derived from the ratio of S IV 1404.8 to S IV 1406.02), this ratio gives densities ranging from $\log n_e/\mathrm{cm}^{-5} = 10.8$–$11.0$. Similarly, a ratio computed for the 1399 and 1401 lines of O IV has values in the range 0.29–0.35, which yields electron densities of $\log n_e/\mathrm{cm}^{-5} = 10.8$–$11.2$.

3. PHYSICAL DRIVERS OF RECURRENT HELICAL JETS

Observations by *SDO*/AIA and *IRIS* establish the case that the jets are homologous and helical in nature. The four jets are homologous in the sense that they share substantial similarity in their observed spatial structure and evolution. This begs the

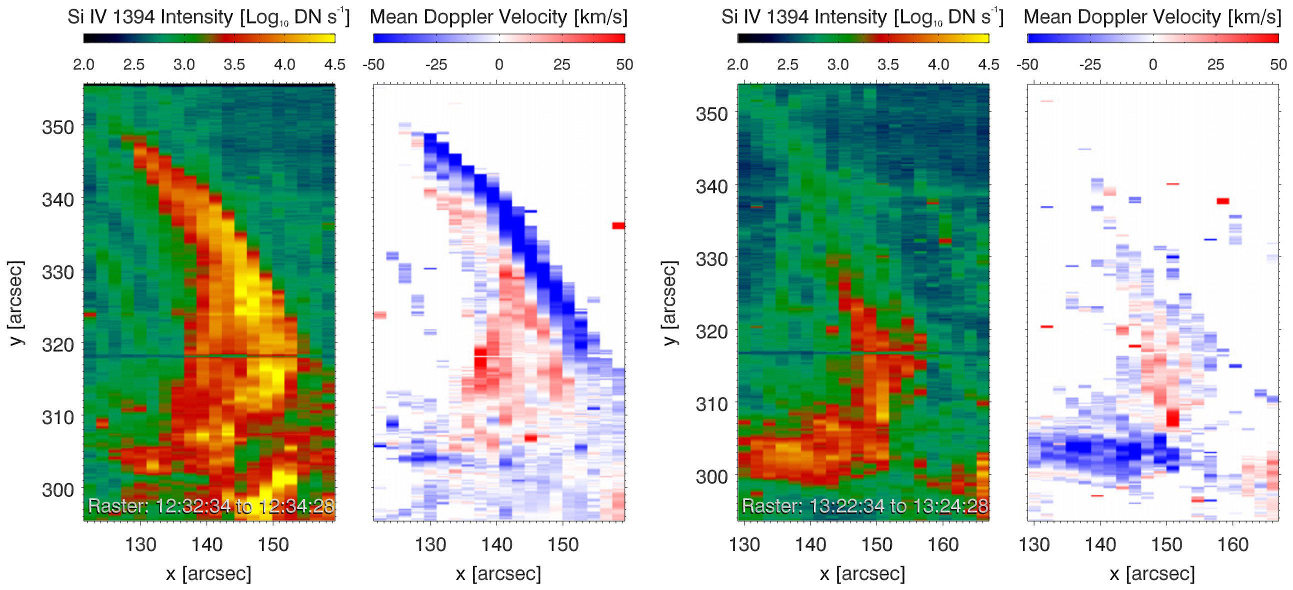

(a) Jet 1 (b) Jet 2

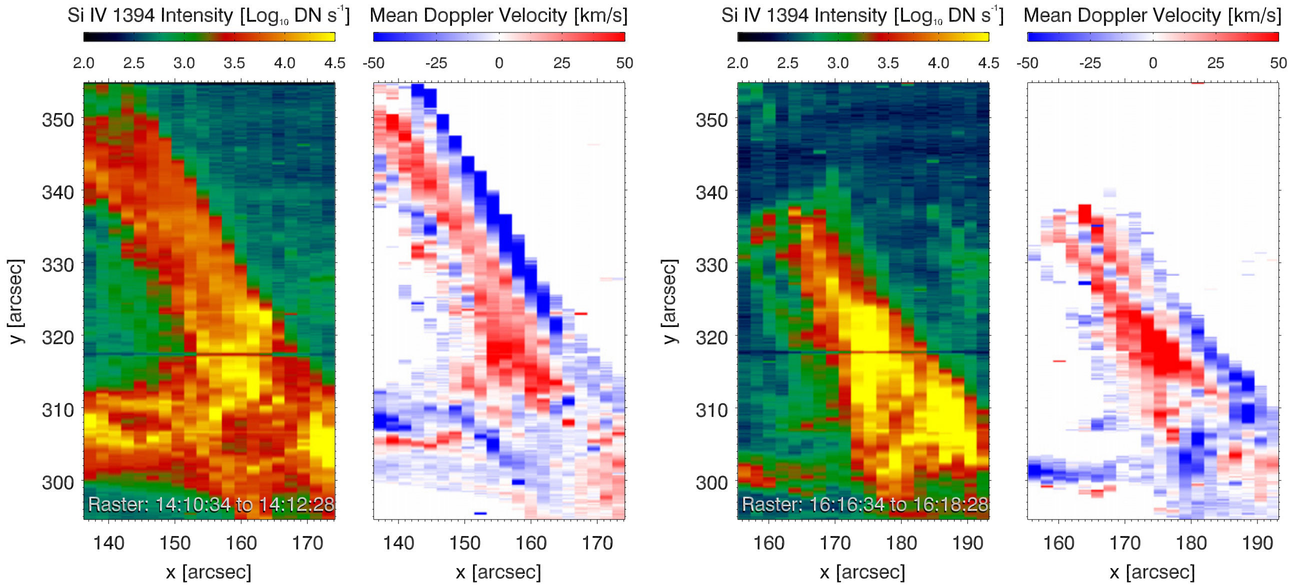

(c) Jet 3 (d) Jet 4

Figure 5. Total intensity and mean Doppler velocity of the four jets as computed from *IRIS* observations of the Si iv 1394 line. In all four jets, there is a tendency for northern edge to be blueshifted while the southern edge is redshifted. This spatial pattern suggests all four jets are helical with the same (negative) sign of kinetic helicity.

question of the underlying driving mechanisms that lead to the initiation of the jets.

There is a large body of work using numerical MHD simulations to study how emergence of magnetic flux into pre-existing coronal field initiates jets (Yokoyama & Shibata 1995; Miyagoshi & Yokoyama 2004; Archontis et al. 2005; Galsgaard et al. 2005; Isobe et al. 2007; Moreno-Insertis et al. 2008; Nishizuka et al. 2008; Heggland et al. 2009; Archontis et al. 2010; Archontis & Hood 2013; Moreno-Insertis & Galsgaard 2013; Takasao et al. 2013; Fang et al. 2014). Most of the simulations focus on single jets following reconnection between the emerging magnetic system with the ambient field. Recent work started to investigate how multiple jets can be emitted from the same source region. From a 3D MHD simulation of flux emergence, Archontis et al. (2010) reported that a series of reconnection events between the emerging flux system and the ambient coronal field led to recurrent jets. Moreno-Insertis & Galsgaard (2013) performed a similar numerical experiment and found a succession of eruptions, some of which have physical properties that resembled the "standard" type of jet while others were miniature flux rope ejections that that may be associated with so-called blowout jets (Moore et al. 2010). While the Moreno-Insertis & Galsgaard (2013) paper mentions that the erupting flux ropes in the simulation seem to rotate as if they were converting twist into writhe, the possible helical motion of the jets themselves were not studied.

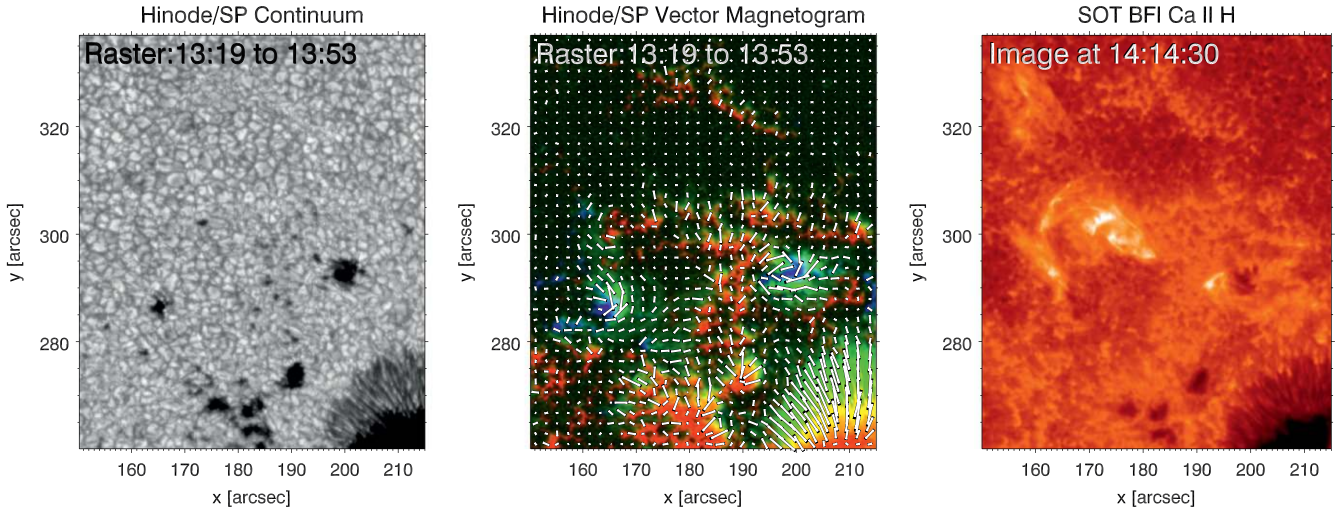
Hinode/SP Continuum

Hinode/SP Vector Magnetogram

SOT BFI Ca II H

Figure 6. *Hinode* SOT observations of the jet-emitting region of AR 11793. Left: continuum image from a *Hinode*/SP raster scan. Center: vector magnetogram of the same field of view. The line of sight component (B_l) of the magnetic field is denoted such that blue and red denote positive and negative polarities, respectively. Green-color coding shows the strength of the transverse component (B_t). Overplotted lines show the orientation of the transverse field. Right: broadband filter (BFI) image in the Ca II H channel during the occurrence of the third jet.

Fang et al. (2014) modeled solar jets by performing 3D MHD simulations of twisted flux tubes emerging into a coronal layer with an ambient inclined field. They included magnetic field-aligned thermal conduction in their model, which provides the dominant mechanism for energy loss by plasma that has been heated to transition region and coronal temperatures. They reported the existence of columnar jets consisting of plasma at a broad range of temperatures (chromospheric to coronal). Due to acceleration by the Lorentz force acting on reconnected field lines, the jet columns exhibit spinning motion. Synthetic intensity-weighted Dopplergrams (using coronal lines) of a simulated jet column from a side perspective gives net Doppler shifts of $\pm 20\ \mathrm{km\ s^{-1}}$ on opposite sides of the columnar jet axis.

Recently, Lee et al. (2015) performed a 3D MHD simulation of the emergence of a strongly twisted flux tube from the convection zone into the atmosphere. They imparted a density deficit distribution to the tube so that two segments of the tube would emerge and interact with each other as well as with the ambient inclined coronal field. The simulation yielded four episodes of twisted flux rope ejections carrying significant mass loads away from the emerging flux region. These flux tubes untwist as they are ejected, resulting in signatures of (revised) torsional Alfvén wave propagation.

Apart from magnetic flux emergence, there is another means by which photospheric magnetic evolution can lead to jets, especially those with rotational motion. One possibility of generating homologous helical jets was investigated by Pariat et al. (2009, 2010). In their numerical MHD studies, the authors considered the scenario in which a circularly shaped patch of magnetic flux is embedded in an environment with a predominantly vertical field of the opposite sign. For convenience let us call the circularly shaped patch of magnetic flux the "parasitic" pole. The initial potential field configuration has a coronal null with a fan that forms a quasi-separatrix (QSL). The QSL separates two magnetic volumes, one consisting of the set of closed field lines connecting the parasitic pole with its surroundings, and an exterior volume consisting of purely open magnetic field lines. About the axis of symmetry of this parasitic pole, they applied rotational motion at a fraction of the local Alfvén speed to mimic twisting of the field due to horizontal photospheric flows. The numerical simulations showed that, given sufficient cumulative rotation (greater than one turn), the magnetic system is driven to a state where reconnection of the magnetic field allows it to impulsively release the stored magnetic energy. A consequence of the relaxation is the formation of a helical jet. Subsequently, continued application of rotational driving at the bottom boundary led to the formation of similar helical jets.

The driving mechanism considered by Pariat et al. (2009, 2010) is in principle different to that of emerging flux in that only horizontal motions at the photosphere is applied. However, the emergence of magnetic flux can also drive systematic horizontal flows that shear already emerged field (Manchester IV 2001; Magara & Longcope 2003; Manchester IV et al. 2004; Magara 2006; Cheung et al. 2010; Fang et al. 2010, 2012; Cheung & Isobe 2014, Section 3.6.3). Emergence-driven shear flows can lead to injection of magnetic energy and magnetic helicity for driving eruptive phenomena, including jets and coronal mass ejections. So the physical mechanism driving the recurrent jets reported here may not be exclusively due to one scenario or the other (i.e., flux emergence versus shearing/rotational motion).

To investigate the underlying physical driver(s) that cause the observed helical jets, we examine observations of the lower atmosphere by *Hinode*/SOT and *SDO*/HMI.

3.1. Lower Atmospheric Observations by Hinode/SOT

Figure 6 shows SOT observations of the jet-emitting region of AR 11793. The left panel shows the continuum intensity image from a *Hinode*/SP raster scan. The central panel shows the vector magnetogram from a Milne–Eddington Stokes inversion (Lites & Ichimoto 2013; Lites et al. 2013). The right panel shows a broadband filter image from the Ca II H channel during the ocurrence of the third jet. The latter shows a set of closed loops and a set of inclined loops pointed toward the northeast direction. The morphology of the loops is somewhat reminiscent of the jet studied by Liu et al. (2009; see Figure 1 of their article). In their paper, they studied SOT observations of a jet using Ca II H images alone. From the morphological evolution, they concluded that the apparent motion of the jet material was consistent with a helical jet with untwisting magnetic field lines. In the case they studied, the jet was observed off the solar limb so the two-part structure comprised of the closed loops and the inclined open loops were not contaminated by background emission. In our case, contribution to the SOT Ca II H channel by emission in the upper photosphere makes it harder to delineate the specific features. Still, the morphological similarities with the case studied by Liu et al. (2009) support their conclusion that their jet exhibited helical motion.

The eastern (left) ends of the closed loops in the Ca II H image appear to be anchored at a compact patch of positive polarity field located at $(x, y) = (165'', 287'')$. Inspection of the accompanying continuum image shows this positive patch to be a pore. This positive polarity pore is embedded in the interior of a supergranule. In contrast, the network field surrounding this supergranule is predominantly negative (the same polarity as the nearby leading spot). In this sense the pore is a parasitic pole. Inspection of the transverse field (i.e., the amplitude of the plane-of-sky component $|B_t|$) shows the presence of a strong horizontal field ($B_t > 700$ G) on the western (right) side of the pore. Furthermore there is a moderate transverse field ($|B_t| \sim 300$ G) pervading a large fraction of the sugergranular cell. The left–right asymmetry of the B_t distribution about the pore is suggestive of electric currents associated with a non-potential magnetic field configuration (more on this in Section 4.1).

Inspection of the temporal sequence of Ca II H images indicates the presence of bright grain pairs that form in the vicinity of the parasitic pore. These bright grain pairs are separated by a dark lane with a length of 1–2 Mm. This type of phenomenon is a robust proxy for emerging flux (e.g., Strous & Zwaan 1999; Cheung et al. 2008; Guglielmino et al. 2010) and their presence in the vicinity of the parasitic pore suggests flux emergence may play a role in driving the recurrent jets.

4. MAGNETIC FIELD EVOLUTION

In this section we investigate how the magnetic field in the source region of the jets evolve, and how this leads to recurrent jet production. For this purpose we use HMI vector magnetograms to drive simplified numerical models of chromospheric and coronal field evolution.

4.1. HMI Vector Magnetograms

The *Hinode*/SP vector magnetogram shown in Figure 6 suggests the presence of electric currents in the photospheric field around the parasitic pore. Due to *Hinode* telemetry limitations, only one SP map is available in the interval containing the four jets. So for the purpose of inspecting the evolution of the photospheric magnetic field, we used vector magnetograms from HMI instead.

Each HMI vector magnetogram is produced by a Milne–Eddington inversion of *IQUV* Stokes maps temporally interpolated over an apodization window spanning 1350 s (Hoeksema et al. 2014). This is done to increase the signal-to-noise ratio of the Stokes parameters and to filter out *p*-mode oscillations. While HMI vector magnetograms are not instantaneous representations of the photospheric field at any given time, the pixels in the same magnetogram are co-temporal. HMI provides vector magnetograms of the full AR at a regular cadence of one frame per 12 minutes. We use vector magnetograms from the HMI data series `hmi.sharp_cea_720s` (Sun 2013). This series provides vector magnetograms in (revised) AR patches, such that the magnetic field vectors have been disambiguated, transformed, and remapped onto a cylindrical equal area grid. The magnetic vector is expressed as (B_r, B_θ, B_ϕ), corresponding to the radial, longitudinal, and latitudinal components, respectively. Since our main region of interest is relatively small ($L \sim 30$ Mm), we ignore the effects of curvature and use the following mapping to a local Cartesian coordinate system $B_\theta \rightarrow B_x$, $B_\phi \rightarrow B_y$, and $B_r \rightarrow B_z$. This enables us to compute the vertical current density

$$j_z = \frac{\partial B_y}{\partial x} - \frac{\partial B_x}{\partial y}. \tag{3}$$

Inspection of maps of j_z during the jet-emitting period reveals a persistent patch of positive j_z near the parasitic (positive polarity) pore. Figure 7 shows HMI vector magnetograms in the neighborhood of the pore at 09:00, 10:46, and 12:34 UT. The left column shows the vertical component B_z. The positive polarity pore is roughly centered at $(x, y) = (-2, 0)$ Mm in all three snaphots. The horizontal magnetic field can be decomposed into the sum of a potential component (calculated from B_z) and a current-carrying component. These are respectively shown in panels in the middle and right columns. A persistent patch of current-carrying field can be found on the west side of the pore at $(x, y) = (-1, 0)$. This feature is also found in the middle panel of Figure 6, which shows the *Hinode*/SP vector magnetogram of the same region. The *Hinode*/SP map provides a more accurate field measurement due to higher spectral coverage and resolution. The strength of the current-carrying horizontal field in this patch reaches 1 kG and exceeds the field strength of the current-free counterpart. This indicates that the magnetic field on the west side of the pore is strongly twisted. Inspection of the B_z time sequence from HMI shows that magnetic flux is emerging in this area. The orientation of the emerging flux is such that negative and positive polarity fields are migrating in roughly the north and south directions, respectively. So both *Hinode*/SP and *SDO*/HMI vector magnetograms give evidence for the emergence of twisted field in the vicinity of the pore. In the following section, we present numerical simulations to investigate how this photospheric driving is related to the phenomenon of recurrent helical jets.

4.2. Numerical Experiments Using a Data-driven Magnetofrictional Model

We use a time-dependent magnetofrictional (Craig & Sneyd 1986; Yang et al. 1986; van Ballegooijen et al. 2000) model to carry out data-driven numerical experiments of coronal field evolution. Under this model, the fluid velocity v appearing in the induction equation is assumed to be proportional to the local Lorentz force $\boldsymbol{j} \times \boldsymbol{B}$. This leads to an evolution of any arbitrary magnetic configuration to relax toward a force-free field. Magnetofriction has been used to model the formation and evolution of filaments (Mackay et al. 2000; van Ballegooijen 2004; Mackay & van Ballegooijen 2006, 2009; Yeates et al. 2007, 2008; Yeates & Mackay 2009), the coronal field above the quiet Sun magnetic carpet (Meyer et al. 2012),

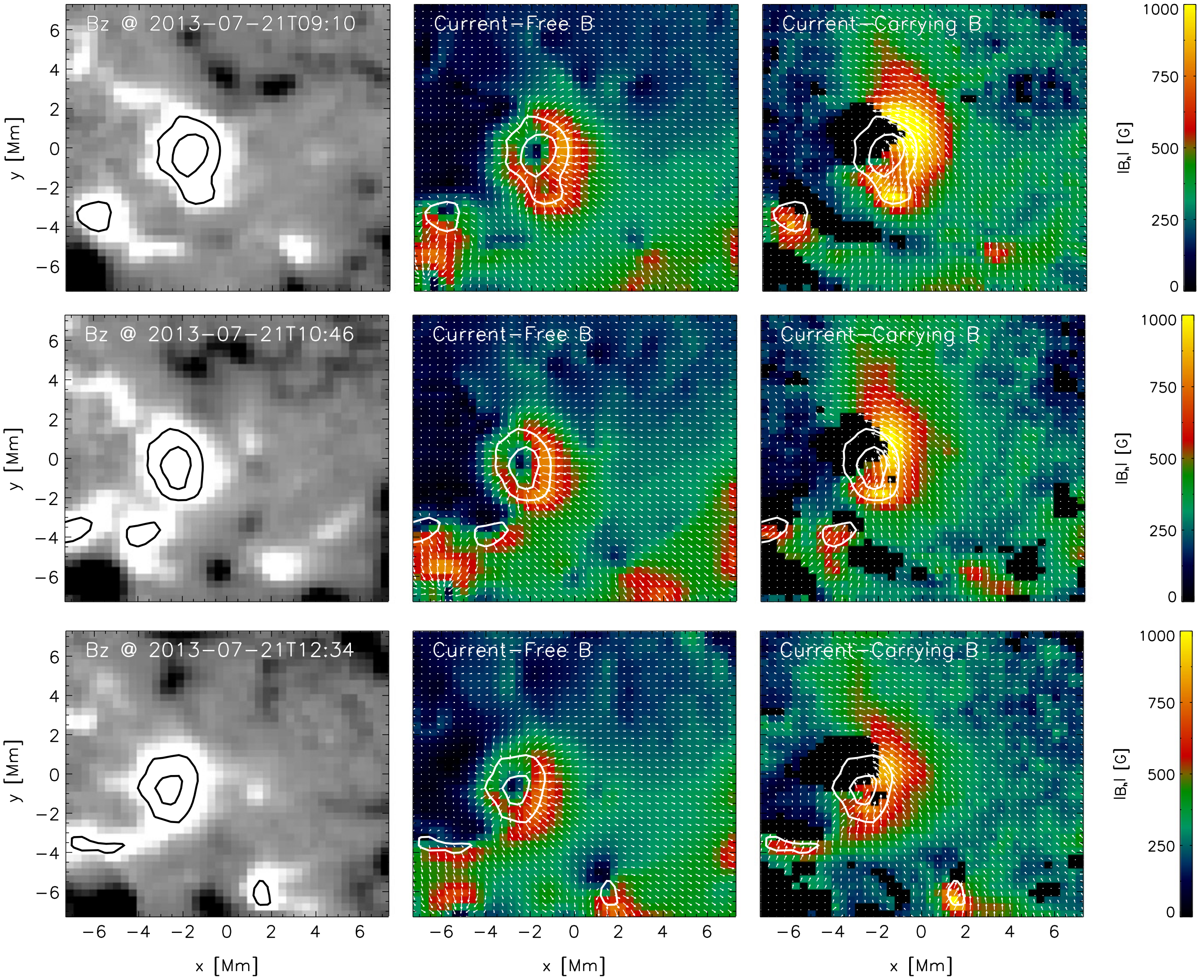

Figure 7. *SDO*/HMI vector magnetograms of the parasitic pore and its surroundings. Left: vertical component of $\boldsymbol{B}$ (grayscale saturated at ±200 Mx cm^{-2}). Middle: horizontal components of the current-free (i.e., potential) part of $\boldsymbol{B}$. Right: horizontal components of the current-carrying part of $\boldsymbol{B}$. A strong, persistent patch of the current-carrying field is found on the west side of the pore. Comparison with the B_z distribution shows this current-carrying patch is coincident with an emerging flux region (just northwest of the parasitic pore). Contours for $B_z = 500$ and 1000 Mx cm^{-2} are shown on all panels to indicate the position of the pore.

and the evolution of ARs (Cheung & DeRosa 2012; Gibb et al. 2014).

Following Cheung & DeRosa (2012), we use a Cartesian magnetofriction code that solves for the vector potential $\boldsymbol{A}$, namely

$$\frac{\partial \boldsymbol{A}}{\partial t} = \boldsymbol{v} \times \boldsymbol{B}, \tag{4}$$

where $\boldsymbol{B} = \nabla \times \boldsymbol{A}$, $\boldsymbol{j} = \nabla \times \boldsymbol{B}$ and

$$\boldsymbol{v} = \frac{1}{\nu} \boldsymbol{j} \times \boldsymbol{B}. \tag{5}$$

The magnetofrictional coefficient ν is given by

$$\nu = \nu_0 B^2 \left(1 - e^{-z/L}\right), \tag{6}$$

where $\nu_0 = 10\,\mathrm{s\,Mm^{-2}}$ and $L = 1.7$ Mm. As described in Cheung & DeRosa (2012), the code uses a staggered grid (Yee mesh) such that $\boldsymbol{A}$ and $\boldsymbol{j}$ are defined at cell edges, $\boldsymbol{B}$ is defined on cell faces, and $\boldsymbol{v}$ is defined at cell centers. The code has been updated to use a van Leer slope limiter (van Leer 1977) to interpolate $\boldsymbol{v}$ onto cell edges when computing the $-\boldsymbol{v} \times \boldsymbol{B}$ electric field. We find that this scheme provides better numerical stability while being less diffusive than explicitly imposing an anomalous resistivity.

4.2.1. Initial and Boundary Conditions

The observed recurrent jets occur in the neighborhood of the ambient inclined field as part of a set of AR loops that connect the leading and following polarities of AR 11793. To capture the large-scale magnetic connectivity, we use a computational domain sufficiently large to encompass the entire AR. The domain spans 248 and 131 Mm in the x (longitudinal) and y (latitudinal) directions, respectively. The bottom boundary is located at $z = 0$ and the top boundary is located at 105 Mm. The horizontal and vertical grid spacings are 364 and 547 km, respectively. The initial condition is a potential field of the AR computed for the magnetogram at 2013 July 21 T06:12 UT ($5^{\mathrm{h}}22^{\mathrm{m}}$ before the start of the *IRIS* observation) and the simulations are evolved forward in time from that state.

As discussed in Cheung & DeRosa (2012), the bottom boundary condition for the magnetofrictional model is given by the transverse components of the photospheric electric field, namely $-\partial_t A_x = E_x$ and $-\partial_t A_y = E_y$. The retrieval of the horizontal electric field from vector magnetograms is a difficult inverse problem (Fisher et al. 2010, 2012). As recently demonstrated by Kazachenko et al. (2014), the incorporation of Doppler flows as a constraint leads to inversion results that accurately reproduce electric fields (and the associated Poynting flux) in an anelastic MHD simulation. The validation of this method for use with vector magnetograms at the resolution and sensitivity of HMI on photospheric magnetic structures is a work in progress.

Instead of attempting to perform a faithful retrieval of the photospheric electric field for this problem, we use a different method to compute electric fields with a given assumption. Given the sequence of input vertical magnetograms B_z, its relation to $\boldsymbol{E}_h = (E_x, E_y)$ is given by the vertical component of the induction equation

$$\frac{\partial B_z(x, y)}{\partial t} = -\hat{z} \cdot \left(\nabla \times \boldsymbol{E}_h\right). \tag{7}$$

In order to solve for $\boldsymbol{E}_h$, another relation must be specified. Specifying the horizontal divergence of the electric field:

$$D(x, y) = \nabla_h \cdot \boldsymbol{E}_h. \tag{8}$$

fully constrains the problem. In our numerical experiments, we assume

$$D(x, y) = j_z(x, y) U_0, \tag{9}$$

where $j_z = (\nabla \times \boldsymbol{B})_z$ is the vertical current density computed at the photosphere. This choice of the functional form for D is motivated by the following scenario. Consider an axisymmetric twisted magnetic flux tube that is invariant along its axis and let the tube axis be parallel to the vertical direction $\hat{z}$. Let the tube rise vertically with $\boldsymbol{v} = U_0\hat{z}$. It can be shown that the divergence of the $-\boldsymbol{v} \times \boldsymbol{B}$ electric field corresponding to this motion is given by Equation (9). By adopting Equation (9), we have chosen to inject twist via the bodily emergence of twisted field (c.f. Leka et al. 1996). To drive the numerical experiments described here, j_z is computed from HMI vector magnetograms and U_0 is a free parameter (with dimensions of velocity). Varying U_0 changes the effective injection speed of magnetic twist (as described by j_z) into the computational domain.

Another possible way to inject twist is by means of shearing and rotational motions in the photospheric plane. In MHD models of the emergence of twisted flux tubes, such flows are accelerated by magnetic torques exerted by the Lorentz force (Longcope & Welsch 2000; Manchester IV et al. 2004; Magara 2006; Fan 2009; Cheung et al. 2010; Fang et al. 2012; Cheung & Isobe 2014). Twist injection by both bodily emergence of current-carrying field and rotational motions in the photosphere are likely present in our region of interest (see Section 3.1). For simplicity, however, we assume in our numerical setup that twist injection is due to the former.[8]

4.2.2. *Results of Numerical Experiments*

We carried out three numerical experiments, one each for $U_0 = 0$, $U_0 = 1.1$, and $U_0 = 2.2\,\mathrm{km\,s^{-1}}$. For the run with $U_0 = 0$, $\boldsymbol{E}_h$ is decoupled from the photospheric distribution of j_z. In this case there is no systematic current injection and we do not find any magnetic field evolution resembling the helical motion of the observed jets. For $U_0 = 1.1\,\mathrm{km\,s^{-1}}$, we find repeated episodes of twisting followed by untwisting in the model magnetic field that shares qualitative similarities with the recurrent jets. Figure 8 shows snapshots of two such homologous episodes of evolution from the model. Row (a) shows B_z at the bottom boundary of the domain, which is constrained to match the B_z observed by HMI. Row (b) shows synthetic chromospheric "magnetograms" (i.e., B_z sampled at $z = 4.5$ Mm). We chose to sample the magnetic field at a height that is above the nominal height range associated with 1D models of the solar chromosphere (∼1 to 2 Mm; e.g., see Withbroe & Noyes 1977; Vernazza et al. 1981) since 3D radiative MHD simulations show that magnetic flux emerging into the atmosphere can lift the chromosphere and transition region layers by a few Mm (Martínez-Sykora et al. 2008). In both cases, the earliest chromospheric magnetogram (i.e., panels (b1) and (b4)) shows a positive polarity feature pressed against a negative polarity feature in a yin-yang pattern. Inspection of the horizontal vectors and the distribution of j_z at that height shows that the field near the polarity inversion line is sheared and carries current. When we inspect subsequent vector magnetograms, we find the horizontal vectors have, on average, rotated in a clockwise direction. This is a result of the untwisting of the magnetic field by a clockwise rotational flow. The vertical component of vorticity for such a flow is negative, consistent with the sign of vorticity of the observed recurrent jets.

To visualize the magnetic field lines, we calculate a scalar proxy emissivity $\epsilon(x, y, z)$ using the following procedure. For each field line traced from a position at the photospheric ($z = 0$) boundary, we compute the following field-line averaged quantity:

$$\langle \mathrm{WD} \rangle = L^{-1} \int_0^L \boldsymbol{F}_{\mathrm{Lorentz}} \cdot \boldsymbol{v} dl, \tag{10}$$

where L is the length of a field line and $\boldsymbol{F}_{\mathrm{Lorentz}} \cdot \boldsymbol{v}$ represents the rate of work done by the Lorentz force. In a full MHD model, $\boldsymbol{F}_{\mathrm{Lorentz}} \cdot \boldsymbol{v}$ appears as a source term in the kinetic energy equation and as a sink term (with negative sign) in the magnetic energy equation. In a magnetofrictional model,

$$\boldsymbol{F}_{\mathrm{Lorentz}} \cdot \boldsymbol{v} = \frac{1}{4\pi\nu} [(\nabla \times \boldsymbol{B}) \times \boldsymbol{B}]^2 \geqslant 0. \tag{11}$$

so that $\langle \mathrm{WD} \rangle \geqslant 0$. If a field line crosses one of the side or top boundaries of the computational domain, we set $\langle \mathrm{WD} \rangle = 0$ so that the field line is not emissive. A magnetic field line will cross a number of cell elements in the computational domain.

---

[8] For the specific case of an axisymmetric flux tube with azimuthal field $B_\theta(r) = qr\, B_l(r)$, where q is the twist parameter and $B_l(r)$ is the longitudinal component of the magnetic field, one can pick parameters for the two scenarios (i.e., bodily transport of twisted field and rotational motion) that result in identical boundary conditions. For such a tube rotating about its axis with an angular velocity ω_0, it can be shown that $\nabla \cdot \boldsymbol{E}_h = -q^{-1}\omega_0 j_z$, which is equivalent to Equation (9) with $U_0 = -q\omega_0$.

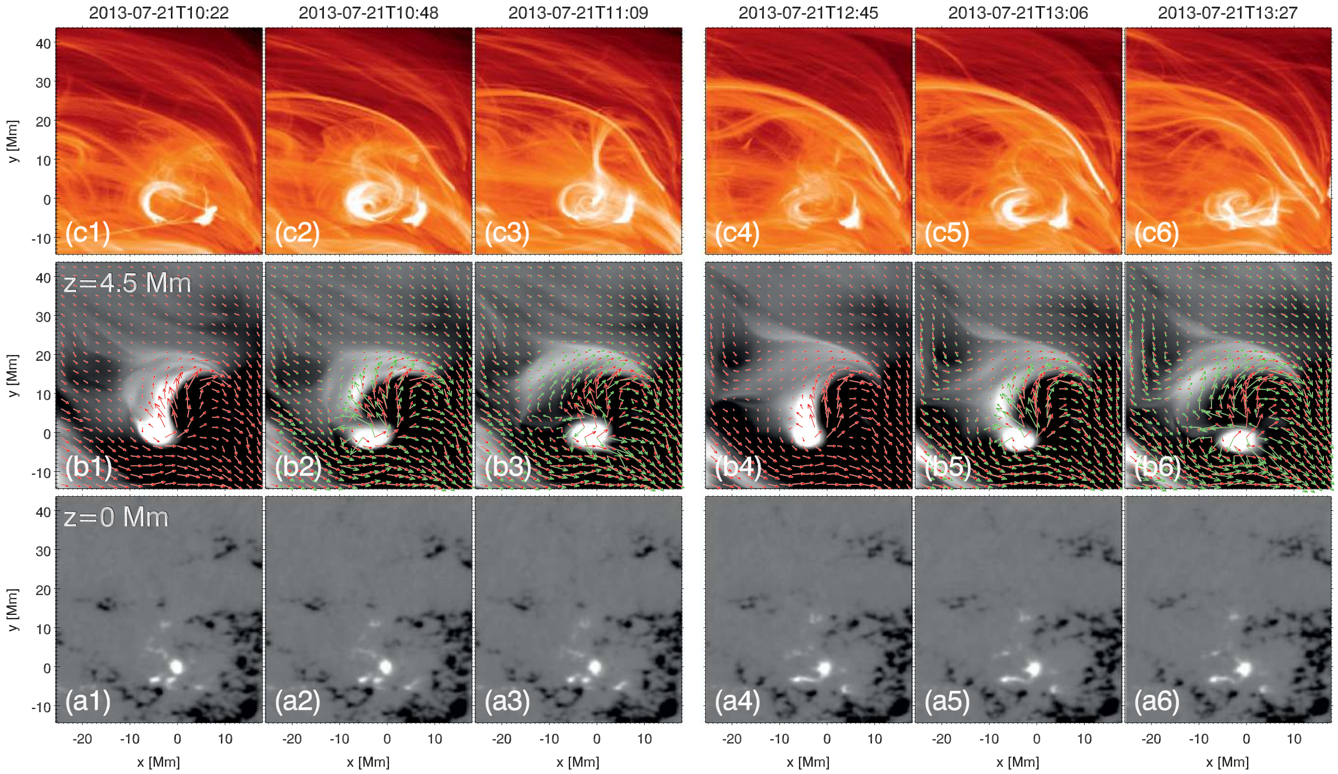

Figure 8. Two examples of untwisting magnetic field in the data-driven model with $U_0 = 1.1$ km s^{-1}. Columns (1)–(3) show a temporal sequence of one such episode while columns (4)–(6) show a homologous episode later in time. In this local coordinate system the parasitic pore is centered at the origin. Row (a) shows the photospheric vertical field $B_z(z = 0)$ scaled between ±800 Mx cm^{-2}. Row (b) shows synthetic chromospheric vector magnetograms at a constant height of $z = 4.5$ Mm. Grayscale shows B_z scaled between ±100 Mx cm^{-2} and red arrows show the horizontal field at the same time. In the left and right sets of panels, the green arrows indicate the horizontal field at 10:48 and 12:45 UT, respectively (i.e., they show the horizontal field at the beginning of each set). The clockwise rotation of the arrows in both cases shows the magnetic field evolved with a clockwise rotation. Row (c) shows a visualization of the field lines according to the proxy emissivity model of Equation (12).

For each of these cell elements, we increment the local value of the emissivity by

$$d\varepsilon = G \langle \mathrm{WD} \rangle \Delta x \Delta y, \tag{12}$$

where G is some arbitrary scale factor (here we use $G = 1$). Row (c) shows integrals of the resulting proxy emissivity along vertical lines of sight. This method allows us to inspect a large number of fields lines (here we traced four field lines per pixel), each lit up according to the field-line averaged rate of magnetic energy loss due to work done by the Lorentz force. The images shown in row (c) are log-scaled so they do not depend on the specific value of the constant G.

Figure 9 shows a 3D visualization of the magnetic structure from the same data-driven simulation ($U_0 = 1.1$ km s^{-1}) at 11:02 UT. The topological structure in this case is similar to those in scenarios examined by Pariat et al. (2009, 2010). In their numerical experiments, a parasitic polarity is embedded in an ambient field that is either vertical (Pariat et al. 2009) or inclined (Pariat et al. 2010). In both cases, the model coronal field has a null point. Associated with the null point is a spine field line connecting the parasitic polarity with the null and a set of magnetic field lines forming a fan locus (i.e., a so-called fan-spine topology; see, e.g., Parnell et al. 1996). As shown in Figure 9, the same type of magnetic skeleton is found in the data-driven model. In this case, the ambient field (with polarity opposite to that of the pore) is concentrated at the supergranular boundary, so the fan field lines emanating from the coronal null are connected to network flux. This type of topology is similar to the one inferred for the (un)twisting jet event studied by Guo et al. (2013) and Schmieder et al. (2013). That event also occurred above a parasitic patch embedded in a supergranule at the edge of an AR.

As demonstrated by the numerical MHD experiments by Pariat et al. (2009, 2010), persistent rotation of the parasitic polarity leads to a series of homologous helical jets. The simplistic MF model used in our data-driven simulations does not solve for the continuity, momentum, or energy equations so the model does not yield plasma ejections. However, one can still examine the magnetic evolution in the data-driven model and find similarities between magnetofrictional evolution and MHD evolution. Figure 10 shows two snapshots from a 3D visualization of the magnetic evolution in the magnetofrictional model with $U_0 = 1.1$ km s^{-1}. At 12:55 UT in the model, the pink field lines reveal a twisted flux rope connecting the parasitic pore with the northwestern edge of supergranule boundary. At 13:37 UT, the field has evolved so that the pink field lines (traced from the same positions) trace out a twisted bundle of inclined field. The sign of magnetic twist in this flux bundle is consistent with the sign of rotation revealed by *IRIS* Doppler mean shift maps shown in Figure 5. That is, the sense of twist in this bundle results in a Lorentz force that drives rotational motion with $\omega_l < 0$ (see Section 2.2).

In the Pariat et al. (2009) model, the parasitic polarity was embedded in an ambient field that is purely vertical. For this setup, they found that the critical number of windings needed to be injected into the system to form a helical jet is $N = 1.4$ (see

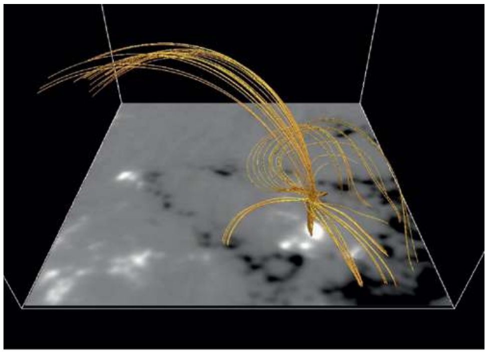

(a) B_z at $z = 0$ Mm

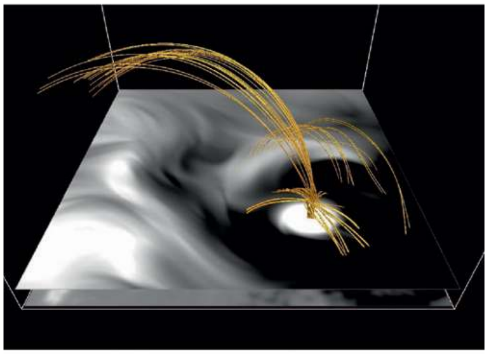

(b) B_z at $z = 4$ Mm

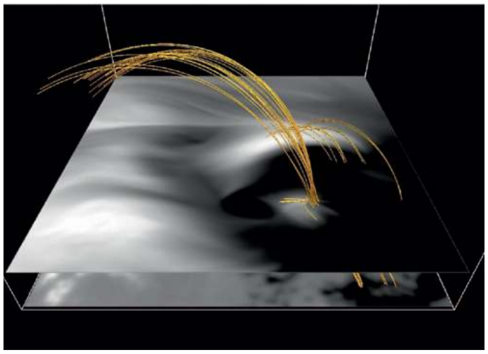

(c) B_z at $z = 8$ Mm

Figure 9. Magnetic configuration in the neighborhood of the parasitic pore in the data-driven model (with $U_0 = 1.1$ km s^{-1}) at time 11:02 UT. Magnetic field lines traced from seed points in the vicinity of a coronal null point reveals a fan-spine topology, with the spine connecting the null point with the underlying parasitic polarity.

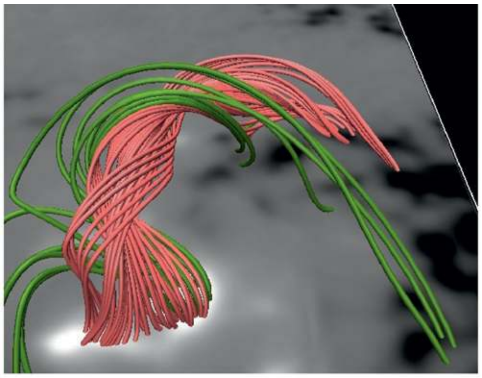

(a) Close-up view of magnetic flux rope at 12:55 UT

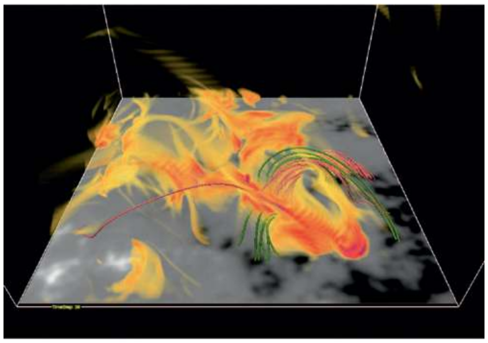

(b) Magnetic field at 12:59 UT

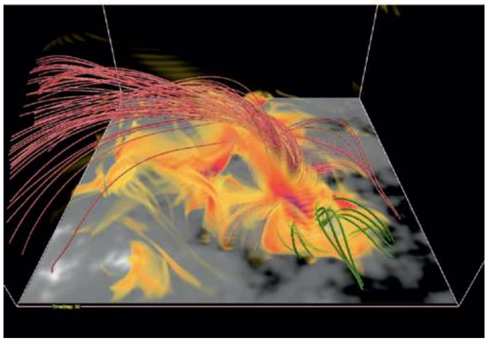

(c) Magnetic field at 13:37 UT

Figure 10. Jet-like magnetic evolution in the data-driven model (with $U_0 = 1.1$ km s^{-1}). Pink magnetic field lines are traced from a stationary grid of points. At 12:55 UT, they show a twisted flux rope structure. At 13:37 UT, field lines traced from the same set of points reveal a set of inclined twisted field lines aligned with the background inclined field. Green field lines are traced from $z = 0$ from the parasitic polarity. The semitransparent orange/red surfaces in panels (b) and (c) indicate regions of strong current density.

also Rachmeler et al. 2010). When the number of windings injected by surface rotation reached this value, the system underwent a helical kink instability, which broke the azimuthal symmetry of the system and generated a helical jet. The exact value of N depends on the geometry of the system. When the ambient open field is inclined, the azimuthal symmetry is no longer present and the critical threshold for injection of twist is lower, with a value of $N = 0.85 \pm 0.1$ (Pariat et al. 2010).

The average length of time required for twisting the field before jet-like reconfigurations occur in the data-driven models is consistent with the findings of Pariat et al. (2010). To estimate the windings injected per unit time in the data-driven simulations, consider an axisymmetric twisted flux tube with longitudinal and transverse components given by

$$B_l(r) = B_0 e^{-r^2/R^2}, \tag{13}$$

$$B_t(r) = \frac{\lambda r}{R} B_0 e^{-r^2/R^2}. \tag{14}$$

Here r is the radial distance from the axis of symmetry, λ is the dimensionless twist parameter, and R is the characteristic radius of the flux tube. This magnetic configuration consists of helical field lines that form concentric flux surfaces about the tube axis. The field lines have magnetic pitch such that the number of turns about the axis (N) over an axial distance d is independent of radial distance r and is given by:

$$N = d\frac{\lambda}{2\pi R}. \tag{15}$$

Consider the scenario in which magnetic twist is injected into the corona by a vertically aligned twisted flux tube rising through the photospheric layer ($z = 0$) with speed U_0. Over a time period Δt, the number of turns injected is $N = U_0\,\Delta t\lambda(2\pi R)^{-1}$. By inspecting the HMI vector magnetograms (Figure 7), we find the horizontal components of the current-carrying field in the vicinity of the parasitic pore to be comparable to the vertical field strength inside the pore (approaching 1 kG). So for rough estimates we can take $\lambda \sim 1$. Taking the size of the pore as $R \sim 1500$ km, we find that the time taken to reach the critical threshold of $N = 0.85$ to be $\Delta t = 2.2 U_0^{-1}$ hr, where U_0 is in units of km s^{-1}. Within the 4 hr period in the simulations (10:00 and 14:00 UT), the number of jet-like reconfigurations in our data-driven simulations with $U_0 = 0$, 1.1, and 2.2 km s^{-1} is 0, 2, and 4, respectively. So the amount of twisting required to drive jet-like episodes in the data-driven model is consistent with what is required in the MHD model of Pariat et al. (2010).

There are limitations to the magnetofrictional models. Although they give us physical guidance about how magnetic energy accumulates and how the magnetic field relaxes by unwinding, the amplitude of velocities in the models is dependent on the free magnetofrictional parameter ν_0. For smaller values of ν_0, the relaxation velocities have higher amplitude. The magnetofrictional models were not fine-tuned to reproduce the Doppler speeds in the observations (generally in our model the speeds are lower by a factor of a few). Furthermore, the relaxation velocity ($\boldsymbol{v} \propto \boldsymbol{j} \times \boldsymbol{B}$) is always perpendicular to $\boldsymbol{B}$, so the model cannot give predictions of the outflow speeds of jet material (from the *IRIS* SJI sequences, the outflow speeds of the jets reach beyond 100 km s^{-1}). Another limitation is the lack of a treatment of thermodynamics quantities such as temperature and density. To overcome these limitations would require data-driven, fully compressible MHD simulations to be performed in future studies. Another valuable exercise would be to compare the amount of twist injection needed in MHD simulations of flux emergence (those yielding helical jets; e.g., Archontis & Hood 2013; Moreno-Insertis & Galsgaard 2013; Fang et al. 2014; Lee et al. 2015) with the results of Pariat et al. (2010).

5. DISCUSSION

Over a 4 hr period on 2013 July 21, recurrent jets emanating from NOAA AR 11793 were simultaneously observed by *IRIS*, *SDO*, and *Hinode*. Doppler shift maps in the *IRIS* Si iv 1394 Å transition region line shows all four jets exhibiting helical motion of the same sign. The *IRIS* Doppler shift maps share considerable resemblance to synthetic Doppler maps in Fang et al. (2014), who carried out MHD simulations of jets resulting from the interaction of a twisting flux tube emerging from the solar convection zone into a coronal layer with ambient inclined field.

Photospheric vector magnetograms from *Hinode*/SOT and *SDO*/HMI show that the source region of the homologous jets consists of predominantly negative polarity field concentrated at the boundary of a supergranule. Embedded inside the supergranule is a parasitic pore with positive magnetic flux. This type of photospheric flux distribution gives a coronal field with a spine-fan topology, which is common in 3D MHD models of coronal jets (e.g., Moreno-Insertis et al. 2008).

Photospheric vector magnetograms from *Hinode*/SP and *SDO*/HMI show a persistent current-carrying magnetic configuration in the vicinity of the parasitic pore. Furthermore, the temporal sequence of vector magnetograms from *SDO*/HMI shows evidence for the emergence of magnetic flux in this current-carrying region (see Section 4.1).

To investigate the driving mechanism for the homologous helical jets, we performed a number of data-driven numerical simulations. All of the numerical simulations are driven by a bottom boundary condition that matches the evolution of the photospheric-B_z as observed by HMI. The temporal sequence of B_z indicates flux emergence is in progress during the time period when helical jets are observed. The occurence of helical jet-like evolution in some simulation runs and not others implies (for this particular case) that the increase in unsigned magnetic flux ($|B_z|$) associated with emerging flux is not a sufficient condition for helical jet formation. What vector magnetograms (Figure 7) reveal is that the emerging flux is current-carrying (i.e., has magnetic twist). In the numerical experiment for which the driving electric fields at the bottom boundary are completely decoupled from the photospheric j_z distribution, we find no helical, jet-like reconfigurations in the magnetic field model. In cases where twisting is imposed (i.e., the driving electric fields are coupled to j_z), the number of jet-like episodes within a 4 hr period increases linearly with the injection parameter U_0 (see Equation (9)). This suggests that the injection of twist via the emergence of current-carrying magnetic field is important for the creation of recurrent helical jets studied here. The amount of twist injection required between successive jet-like episodes is consistent with the findings of Pariat et al. (2010), who carried out fully compressible MHD simulations to model the formation of homologous helical jets. In their numerical experiments, twist injection is due purely to rotational motion in the photosphere. However, MHD simulations of flux emergence from the convection zone into the atmosphere (e.g., Archontis & Hood 2013; Moreno-Insertis & Galsgaard 2013; Fang et al. 2014; Lee et al. 2015) also show signs of twist injection (by both bodily emergence of current-carrying field and Lorentz-force driven rotational motions) followed by emission of helical jets. It is likely both contributions are present for the observed helical jets studied here (which are found above a region of emerging flux).

This work is an example of how complementary observations from multiple observatories can be used in tandem with data-driven modeling to investigate the dynamics of the solar atmosphere. Co-spatial and simultaneous observations from *IRIS*, *SDO*, and *Hinode* provide evidence for the helical nature of the recurrent jets and reveal the magnetic environment of their source region. The use of HMI vector magnetograms to perform data-driven simulations allowed us to investigate how processes such as flux emergence drive coronal evolution. The data-driven simulations were carried out with a magnetofrictional model, which is able to capture how a magnetic configuration relaxes in response to the Lorentz force. However, the model lacks substantial physics and is not suitable for answering questions related to how the stored magnetic energy is used to heat previously cool plasma to transition region and coronal temperatures, and how the plasma ejected along the jet is accelerated. For example, an important question regarding jets is whether the ascending material is directly accelerated by the Lorentz force in reconnected field lines, or whether it is due to chromospheric evaporation, slow mode waves, or upward propagating shocks (e.g., see Takasao et al. 2013). Some of these outstanding issues will likely be addressed in the near future by more detailed analyses of *IRIS* spectra of chromospheric and transition region lines. Going forward, an improvement over the present study would involve data-driven, fully compressible MHD simulations (see Bourdin et al. 2013 for an example of data-driven MHD modeling applied to quasi-steady AR coronal loops). Measurements of the vertical gradients of the magnetic field from vector magnetograms at two heights (photosphere and chromosphere) will help retrieve the driving electric field, but advances in deriving consistent boundary conditions in terms of the appropriate mass, momentum, and energy fluxes are also needed. The ability to do so will allow us to strengthen the constraints imposed by observations (e.g., in terms of temperature and density diagnostics) on theory and to better interpret observations based on realistic physical models.

Data are courtesy of the science teams of *IRIS*, *SDO*, and *Hinode*. *IRIS* is a NASA small explorer mission developed and operated by LMSAL with mission operations executed at NASA Ames Research center and major contributions to downlink communications funded by the Norwegian Space Center (NSC, Norway) through an ESA PRODEX contract. This work is supported by NASA under contract NNG09FA40C (*IRIS*), the European Research Council grant agreement No. 291058, and contract 8100002705 from LMSAL to SAO.

Additionally, M.C.M.C. acknowledges support from NASA's *SDO*/AIA (NNG04EA00C) and *Hinode*/SOT (NNM07AA01C) contracts and grants (NNX14AI14G and NNX13AJ96G) to LMSAL. AIA is an instrument on board the Solar Dynamics Observatory, a mission for NASA's Living With a Star program. *Hinode* is a Japanese mission developed and launched by ISAS/JAXA, collaborating with NAOJ as domestic partner, and NASA and STFC (UK) as international partners. Science operation of *Hinode* is conducted by the *Hinode* science team organized at ISAS/JAXA. Postlaunch operation support is provided by JAXA and NAOJ (Japan), STFC (UK), NASA, ESA, and NSC (Norway).

The numerical modeling work is made possible by NASA's High-End Computing Program. The simulations presented in this paper were carried out on the Pleiades cluster at the Ames Research Center.

REFERENCES

Archontis, V., & Hood, A. 2013, ApJL, 769, L21

Archontis, V., Moreno-Insertis, F., Galsgaard, K., & Hood, A. 2005, ApJ, 635, 1299

Archontis, V., Tsinganos, K., & Gontikakis, C. 2010, A&A, 512, L2

Boerner, P., Edwards, C., Lemen, J., et al. 2012, SoPh, 275, 41

Bourdin, P.-A., Bingert, S., & Peter, H. 2013, A&A, 555, A123

Chae, J., Qiu, J., Wang, H., & Goode, P. 1999, ApJL, 513, L75

Chandra, R., Gupta, G. R., Mulay, S., & Tripathi, D. 2015, MNRAS, 446, 3741

Cheung, M., & DeRosa, M. 2012, ApJ, 757, 147

Cheung, M., Rempel, M., Title, A., & Schüssler, M. 2010, ApJ, 720, 233

Cheung, M., Schüssler, M., Tarbell, T., & Title, A. 2008, ApJ, 687, 1373

Cheung, M. C. M., & Isobe, H. 2014, LRSP, 11, 3

Chifor, C., Isobe, H., Mason, H., et al. 2008, A&A, 491, 279

Cirtain, J., Golub, L., Lundquist, L., et al. 2007, Sci, 318, 1580

Craig, I., & Sneyd, A. 1986, ApJ, 311, 451

Curdt, W., & Tian, H. 2011, A&A, 532, L9

De Pontieu, B., Title, A. M., Lemen, J. R., et al. 2014, SoPh, 289, 2733

Fan, Y. 2009, ApJ, 697, 1529

Fang, F., Fan, Y., & McIntosh, S. W. 2014, ApJL, 789, L19

Fang, F., Manchester, W., IV, Abbett, W., & van der Holst, B. 2010, ApJ, 714, 1649

Fang, F., Manchester, W., IV, Abbett, W., & van der Holst, B. 2012, ApJ, 745, 37

Fisher, G., Welsch, B., & Abbett, W. 2012, SoPh, 277, 153

Fisher, G., Welsch, B., Abbett, W., & Bercik, D. 2010, ApJ, 715, 242

Galsgaard, K., Moreno-Insertis, F., Archontis, V., & Hood, A. 2005, ApJL, 618, L153

Gibb, G. P. S., Mackay, D. H., Green, L. M., & Meyer, K. A. 2014, ApJ, 782, 71

Guglielmino, S., Bellot Rubio, L., Zuccarello, F., et al. 2010, ApJ, 724, 1083

Guo, Y., Démoulin, P., Schmieder, B., et al. 2013, A&A, 555, A19

Harrison, R. A., Sawyer, E. C., Carter, M. K., et al. 1995, SoPh, 162, 233

Heggland, L., de Pontieu, B., & Hansteen, V. 2009, ApJ, 702, 1

Hoeksema, J. T., Liu, Y., Hayashi, K., et al. 2014, SoPh, 289, 3483

Isobe, H., Tripathi, D., & Archontis, V. 2007, ApJL, 657, L53

Kazachenko, M. D., Fisher, G. H., & Welsch, B. T. 2014, ApJ, 795, 17

Kosugi, T., Matsuzaki, K., Sakao, T., et al. 2007, SoPh, 243, 3

Landi, E., Del Zanna, G., Young, P. R., Dere, K. P., & Mason, H. E. 2012, ApJ, 744, 99

Lee, E. J., Archontis, V., & Hood, A. W. 2015, ApJL, 798, L10

Leka, K., Canfield, R., McClymont, A., & van Driel-Gesztelyi, L. 1996, ApJ, 462, 547

Lemen, J. R., Title, A. M., Akin, D. J., et al. 2012, SoPh, 275, 17

Lites, B. W., & Ichimoto, K. 2013, SoPh, 283, 601

Lites, B. W., Akin, D. L., Card, G., et al. 2013, SoPh, 283, 579

Liu, W., Berger, T. E., Title, A. M., & Tarbell, T. D. 2009, ApJL, 707, L37

Longcope, D., & Welsch, B. 2000, ApJ, 545, 1089

Mackay, D. H., Gaizauskas, V., & van Ballegooijen, A. A. 2000, ApJ, 544, 1122

Mackay, D. H., & van Ballegooijen, A. A. 2006, ApJ, 641, 577

Mackay, D. H., & van Ballegooijen, A. A. 2009, SoPh, 260, 321

Magara, T. 2006, ApJ, 653, 1499

Magara, T., & Longcope, D. 2003, ApJ, 586, 630

Manchester, W., IV 2001, ApJ, 547, 503

Manchester, W., IV, Gombosi, T., DeZeeuw, D., & Fan, Y. 2004, ApJ, 610, 588

Martínez-Sykora, J., Hansteen, V., & Carlsson, M. 2008, ApJ, 679, 871

Meyer, K. A., Mackay, D. H., & van Ballegooijen, A. A. 2012, SoPh, 278, 149

Miyagoshi, T., & Yokoyama, T. 2004, ApJ, 614, 1042

Moore, R., Cirtain, J., Sterling, A., & Falconer, D. 2010, ApJ, 720, 757

Moreno-Insertis, F., & Galsgaard, K. 2013, ApJ, 771, 20

Moreno-Insertis, F., Galsgaard, K., & Ugarte-Urra, I. 2008, ApJL, 673, L211

Nishizuka, N., Shimizu, M., Nakamura, T., et al. 2008, ApJL, 683, L83

Pariat, E., Antiochos, S., & DeVore, C. 2010, ApJ, 714, 1762

Pariat, E., Antiochos, S. K., & DeVore, C. R. 2009, ApJ, 691, 61

Parnell, C. E., Smith, J. M., Neukirch, T., & Priest, E. R. 1996, PhPl, 3, 759

Patsourakos, S., Pariat, E., Vourlidas, A., Antiochos, S., & Wülser, J.-P. 2008, ApJL, 680, L73

Pesnell, W. D., Thompson, B. J., & Chamberlin, P. C. 2012, SoPh, 275, 3

Pike, C. D., & Mason, H. E. 1998, SoPh, 182, 333

Rachmeler, L. A., Pariat, E., DeForest, C. E., Antiochos, S., & Török, T. 2010, ApJ, 715, 1556

Savcheva, A., Cirtain, J., Deluca, E., et al. 2007, PASJ, 59, 771

Scherrer, P. H., Schou, J., Bush, R. I., et al. 2012, SoPh, 275, 207

Schmieder, B., Guo, Y., Moreno-Insertis, F., et al. 2013, A&A, 559, A1

Schou, J., Borrero, J. M., Norton, A. A., et al. 2012, SoPh, 275, 327

Shibata, K., Nitta, N., Strong, K. T., et al. 1994, ApJL, 431, L51

Shibata, K., Ishido, Y., Acton, L., et al. 1992, PASJ, 44, L173

Shimojo, M., Hashimoto, S., Shibata, K., et al. 1996, PASJ, 48, 123

Strous, L., & Zwaan, C. 1999, ApJ, 527, 435

Sun, X. 2013, arXiv:1309.2392

Takasao, S., Isobe, H., & Shibata, K. 2013, PASJ, 65, 62

Tian, H., McIntosh, S. W., Xia, L., He, J., & Wang, X. 2012, ApJ, 748, 106

Tsuneta, S., Ichimoto, K., Katsukawa, Y., et al. 2008, SoPh, 249, 167

van Ballegooijen, A. A. 2004, ApJ, 612, 519

van Ballegooijen, A. A., Priest, E. R., & Mackay, D. H. 2000, ApJ, 539, 983

van Leer, B. 1977, JCoPh, 23, 276

Vernazza, J. E., Avrett, E. H., & Loeser, R. 1981, ApJS, 45, 635

Wilhelm, K., Curdt, W., Marsch, E., et al. 1995, SoPh, 162, 189

Withbroe, G. L., & Noyes, R. W. 1977, ARA&A, 15, 363

Yang, W., Sturrock, P., & Antiochos, S. 1986, ApJ, 309, 383

Yeates, A. R., & Mackay, D. H. 2009, SoPh, 254, 77

Yeates, A. R., Mackay, D. H., & van Ballegooijen, A. A. 2007, SoPh, 245, 87

Yeates, A. R., Mackay, D. H., & van Ballegooijen, A. A. 2008, SoPh, 247, 103

Yokoyama, T., & Shibata, K. 1995, Natur, 375, 42